

Towards to Robust and Generalized Medical Image Segmentation Framework

Yurong Chen, *Member, IEEE*, Hui Zhang, *Member, IEEE*, Yaonan Wang, Lizhu Liu
Q. M. Jonathan Wu, *Senior Member IEEE*, Yimin Yang, *Senior Member IEEE*

Abstract—To mitigate the radiologist’s workload, computer-aided diagnosis with the capability to review and analyze medical images is gradually deployed. Deep learning-based region of interest segmentation is among the most exciting use cases. However, this paradigm is restricted in real-world clinical applications due to poor *robustness* and *generalization*. The issue is more sinister with a lack of training data. In this paper, we address the challenge from the representation learning point of view. We investigate that the collapsed representations, as one of the main reasons which caused poor robustness and generalization, could be avoided through transfer learning. Therefore, we propose a novel two-stage framework for robust generalized segmentation. In particular, an unsupervised Tile-wise AutoEncoder (T-AE) pretraining architecture is coined to learn meaningful representation for improving the generalization and robustness of the downstream tasks. Furthermore, the learned knowledge is transferred to the segmentation benchmark. Coupled with an image reconstruction network, the representation keeps to be decoded, encouraging the model to capture more semantic features. Experiments of lung segmentation on multi chest X-ray datasets are conducted. Empirically, the related experimental results demonstrate the superior generalization capability of the proposed framework on unseen domains in terms of high performance and robustness to corruption, especially under the scenario of the limited training data.

Index Terms—Image Segmentation, Representation Learning, Robustness, Generalization.

I. INTRODUCTION

A. Background

At the core bedrock of human intelligence is the character of robust generalization: we have the capability to learn a concept of things and apply it across various tasks and conditions. As Dr. Bengio talked in [1]: “the central challenge

This work is supported in part by the National Natural Science Foundation of China under Grant 61971071, Grant 62027810, in part by the National Key R&D Program of China under Grant 2018YFB1308200.

Y. Chen, H. Zhang, Y. Wang, L. Liu are with the National Engineering Laboratory of Robot Visual Perception and Control Technology, School of Robotics, Hunan University, Changsha, Hunan, 410082 CN (e-mail: chenyrong1998@outlook.com, zhanghuihy@126.com, yaonan.liulz@hnu.edu.cn). Corresponding author: Hui Zhang.

Q. M. J. Wu is with the Department of Electrical and Computer Engineering, University of Windsor, Windsor, Ontario, N9B3P4 Canada (e-mail: jwu@uwindsor.ca).

Y. Yang is with the Department of Computer Science, Lakehead University, Ontario, P7B 5E1, Canada, also with the Vector Institute, Toronto, M5G 1M1, Canada. (e-mail: yyang48@lakeheadu.ca).

in machine learning is that we must perform well on new, previously unseen inputs — not just those on which our model was trained”, modern machine learning-based techniques are ambitious to replicate this phenomenon. Thanks to the development of large datasets and the high-performance computing hardware [2] [3] [4] [5], recent algorithms can capture the general-purpose visual representations which are beneficial to inference on diverse unseen samples.

Even though the existing methods and systems are effective in their tasks [6] [7], however, the desired generalization capability and robustness are only valid under the independent and identically distributed (i.i.d) datasets assumption. If there is a domain-shift between the test data distribution and the training one, the performance dramatically degrades. Unfortunately, the circumstance is common in practical applications. Taking the medical image segmentation task as an example, due to the different equipment protocols and variation of samples across patients, the actual distribution of the training dataset is somehow different from that of the testing set [8] [9]. If there is no guarantee of the model robust generalization, directly applying the trained segmentation model on unseen data would harm the generalization performance. Moreover, the information of the test data is usually inaccessible as the data privacy, during the training phase. Therefore, it is vital to ensure that systems are indeed robust generalization with the limited training data.

B. Motivation and Problem Setting

Recently, domain generalization (DG) is an active research area, which aims to capture the discriminative yet domain-irrelevant representations from one or several different but related datasets and utilizes the learned prior knowledge on the unseen target domains [10] [11] [12]. The model generalization is improved with the domain-shared features. The existing DG methods have demonstrated that they can be investigated through regularization of the embedding space [13], such as minimizing probability distribution divergence between the marginal of data sources; meta-learning [14], e.g., by dividing the training data into meta-train and meta-test sets to mimic the domain-shift. However, the promising idea is hard to afford useful lessons for medical analysis systems. The main impediment is that the extra ample annotated source data are difficult to acquire due to the lack of experts available for annotation, privacy issues, and poor standardization [15]. In

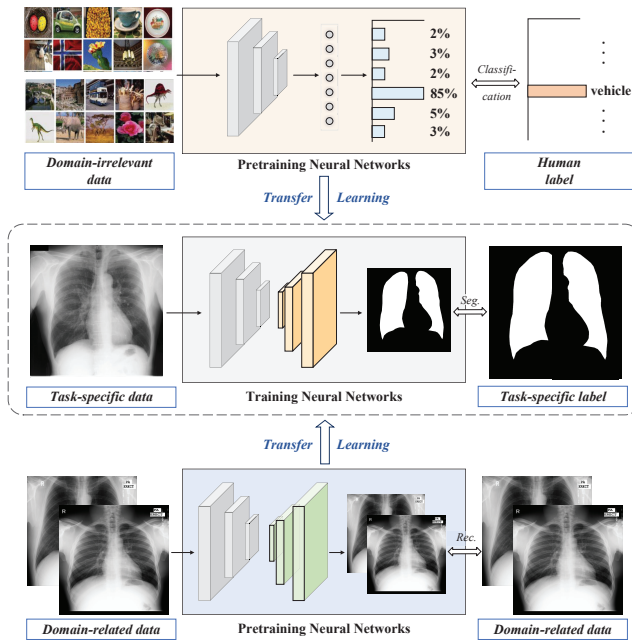


Fig. 1: The comparison of three types of the training process for neural networks. Training from scratch; transfer learning from ImageNet [4]; transfer learning from the domain-related data. (Seg. is segmentation, Rec. denotes reconstruction)

addition, DG needs complex techniques and carefully hyper-parameter tuning, bringing obstacles for applicable medical image segmentation.

Unlike the problem definition of DG, the setting of transfer learning is more prevalent in real-world scenarios. Multiple task-related annotated source medical datasets do not allow access, while a few labeled target domain data are available. Therefore, researchers tune to utilize the transfer learning technique to explore the potential of limited annotated data [16] [17]. Compared with training from scratch (as Fig. 1 shown), the transfer learning generally follows the pretraining-finetuning framework to mitigate the over-fitting problem. The neural networks are pre-trained on the large supervised yet domain-irrelevant datasets (e.g., ImageNet [4] or Places [5]) to perform classification, firstly. The learned representations are transferred into the target task, then finetuning with limited annotated data to polish the model generalization and robustness. With this tide, the transfer learning achieves remarkable performance on medical image segmentation [16] [18], lesion detection [17], etc.

However, He et al. [19] reports that the performance of using standard models trained from scratch yields similar with their ImageNet pretraining counterparts. In other words, the pretraining only speeds up the convergence and does not contribute to the model inference capability. That motivates us to think what the real effect of pretraining on medical image processing. In particular, we focus on two problems: (i) is the pretraining necessary for the downstream tasks, such as medical image segmentation; (ii) is there a gap of knowledge learned from the natural image on pretraining and the medical data on downstream tasks.

C. Contribution

To answer the first question, we compare the performance of training from scratch strategy and pretraining-finetuning on lung segmentation. Several the-state-of-art pretraining methods, including supervised classification [20], pretext tasks-based [21] [22] [23], and contrastive learning-based self-supervised learning [24] [25] [26] [27] are investigated. The pretraining does not substantially improve accuracy, however, we notice that it has an impact on the performance of model generalization and robustness. Following the research work [28] [29], the robustness tests are conducted on corrupted inputs. For the generalization capability tests, we utilize three heterogeneous chest X-ray datasets that one for training, others for testing. Empirically, comprehensive experiments prove the pretraining is necessary.

To answer the second problem, we discuss the robustness and generalization of models that are pretrained on the general natural image and on the domain-related medical data. It is obvious that the medical image, such as X-ray, differs from the general data and it is gray-scale and has similar spatial structures across images. Therefore, the knowledge learned from the natural images may be inferior to transfer on the medical images, which limits the applicability of existing pretraining approaches. In addition, if the network architecture changes, the pretrained model cannot be utilized.

Considering the above problems, in this paper, we propose a pretraining-finetuning robust generalized medical image segmentation framework, as shown in Fig. 2. In particular, while the expert annotated target domain data is rare, the public related unlabeled datasets are available. We would like to leverage these data to extracting valuable representation during the pretraining phase. Unlike previous unsupervised methods, e.g., contrastive learning [30], the generative modelling is theoretically elegant and easy to optimize. We propose a novel Tile-wise AutoEncoder (T-AE) pretraining architecture coupled with solving the *jigsaw puzzle* to learn a representation that exposes important semantic features. In addition, we show the reconstruction branch has a beneficial effect on the downstream network. We design an autoencoder-based auxiliary task to further improve the performance.

Finally, our contributions can be summarized as follows:

- (i) We show that pretraining is necessary for medical image analysis systems. Although it cannot significantly improve the model accuracy on the trained dataset, it has a positive effect on the inference of unseen heterogeneous domains and corrupted inputs. Moreover, we present the pretraining on the ImageNet is inferior to the domain-related data one.
- (ii) We propose T-AE architecture for pretraining on the unlabeled domain-related data to learn meaningful representations. This is a simple yet effective method based on the analysis-synthesize of the observed data belief. With solving *jigsaw puzzle* as the auxiliary task, the latent codes can capture both global and local information, which encourages the network to understand the attributes of data.
- (iii) In this end, the reconstruction approach is employed on the downstream task to further improve the model performances by preventing the collapsed latent feature.

Experiments are conducted on multiple chest X-ray datasets to demonstrate the generalization capability and robustness of the proposed segmentation framework. Moreover, our paper can trigger and inspire further research works.

II. RELATED WORK

A. Medical Image Segmentation

Segmentation of medical images is a fundamental part of any computer-aided diagnosis (CAD) system. Deep learning-based methods have made overwhelming achievements in this field. Recently, the segmentation network architecture designing has been attracted the interest of researchers. U-shaped convolutional neural networks (CNNs) have earned outstanding performance and become the most popular methods [31]. Motivated by the U-shaped network, a dual UNet is designed to segment the lung from cross-manufacturer chest X-ray [32]. Moreover, the DeepLab V3+ architecture [33] is proposed based on the atrous convolutions and pooling operators, and the conditional random field (CRF) post-processing technique. PSPNet [34] as the winner of the ImageNet scene segmentation challenge has received medical imaging researchers' attention [35]. These the-state-of-art baseline segmentation methods provide the basics of further works. Rashid [36] utilizes the fully CNNs to perform lungs segmentation. A nonrigid registration-driven lung segmentation technique is introduced by Candemir et al. [37].

B. Pretraining Methods

Aside from segmentation network studies, transfer learning is widely used in medical image analysis to improve the performance [16] [17], which follows the pretraining-finetuning process. Here, the pretrained model can provide a better initialization for the target task. Previous studies focus on transferring from natural images (e.g., ImageNet) to medical image analysis [2] [3] [18]. The neural networks, e.g., ResNet-50 [20], are pretrained for classification ImageNet [20], firstly. Moreover, unsupervised (self-supervised) learning for pretraining focuses on the problem of learning meaningful representations without expert annotations. The key part of self-supervised learning is to design a suitable pretext task. For example, Norooze et al. design solving *jigsaw puzzles* as the pretext task [21]. Visual representations are learned with a fully convolution neural network through the process of colorizing gray-scale images [22]. The rotating angles of the whole images are designed as a supervision signal for training the network [23]. Recently, the contrastive learning, including SwAV [24], BYOL [25], SimCLR [26], and MoCo [27], have presented overwhelming achievements on various computer vision benchmarks. In particular, SwAV [24] introduces multi-view data augmentation and online clustering strategies into contrastive objectives. MoCo [27] leverages instance-level discrimination via momentum contrast. SimCLR [26] follows MoCo's architecture and introduces more data augmentation methods. BYOL [25] discards negative sampling in contrastive learning. These studies mainly focus on pretraining on the domain-irrelevant data (i.e., natural general image).

C. Generative Models

Unlike contrastive self-supervised learning, generative models also have found their way to the forefront edge of representation learning in the last decade. With the development of the back-propagated-based deep learning, generative adversarial networks (GANs) [38] and Variational autoencoders (VAEs) [39] govern the generative models. GANs consist of a discriminator \mathcal{D} and a generator \mathcal{G} , which can be optimized simultaneously as a zero-sum game. Based on GANs, Cenggoro [40] proposes class expert GAN (CE-GAN) for pretraining that can mitigate the imbalanced class problem. However, GANs have innate shortcomings which are hard to train. VAEs [39], rooted in Bayesian inference, are theoretically elegant and easy to train. VAEs not only recover the data space \mathcal{X} from \mathcal{Z} , but estimate the true data distribution $p_{data}(x)$. This is a simple yet effective method to encoded the prior knowledge into the network. Motivated by this, Newell et al. [41] investigate the effect of the VAEs-pretrained model on downstream tasks.

III. METHOD

The recent medical image segmentation methods pay little attention to the model generalization and robustness, which should be significantly staple when applying the model to the real-world scenario. In this paper, we investigate the robust generalized lung segmentation model endowed by transfer learning, in particular, transferring knowledge from the unlabeled domain-related data. In this section, we formulate the problem of segmentation and the auxiliary representation learning in Section III.A. Secondly, the proposed pretraining method is discussed in Section III.B. Further, we present the improved segmentation network in Section III.C.

A. Problem Formulation and Notation

This work considers two problems: the main one is the lung segmentation from the chest X-ray image; the auxiliary problem is to learn the meaningful representations. Discussing in order, the task-specific dataset T_S consists of N cases ($T_S = \{(x_1, y_1), (x_2, y_2), \dots, (x_N, y_N)\}$), where $x_N \in \mathbb{R}^{H \times W \times C}$ is independent and identically distributed input image sampled from target domain manifold \mathcal{X}_{T_S} in Euclidean space with the height H , width W , and channel C . The corresponding label $y_N \in \mathbb{R}^{H \times W \times 1}$ denotes the mask of the lung, which comprises the pixel set of lung area $\{y_N^{11}, y_N^{12}, \dots, y_N^{hw}\}$, which is form the label space manifold \mathcal{Y} . Based on the fully convolutional neural network-based segmentation framework, we construct an encoder network $f_\varphi(\cdot) : \mathcal{X} \rightarrow \mathcal{Z}$ for feature extraction and a segmentation decoder network $f_s(\cdot) : \mathcal{Z} \rightarrow \mathcal{Y}$, where \mathcal{Z} is the representation space.

The auxiliary problem considers utilizing the domain-related dataset D_r to learn the transferable and meaningful representations. D_r is easy to obtain in public if we waive the need for labels. Therefore, assuming D_r only including M samples ($D_r = \{x_1, x_2, \dots, x_M\}$ where $x_M \in \mathcal{X}_{D_r}$). The core objective of this paper is to learn a neural network to model the data distribution of D_r (i.e., $p_{D_r}(x)$) for realizing representation learning. Following the segmentation network architecture and the philosophy of autoencoder, the network

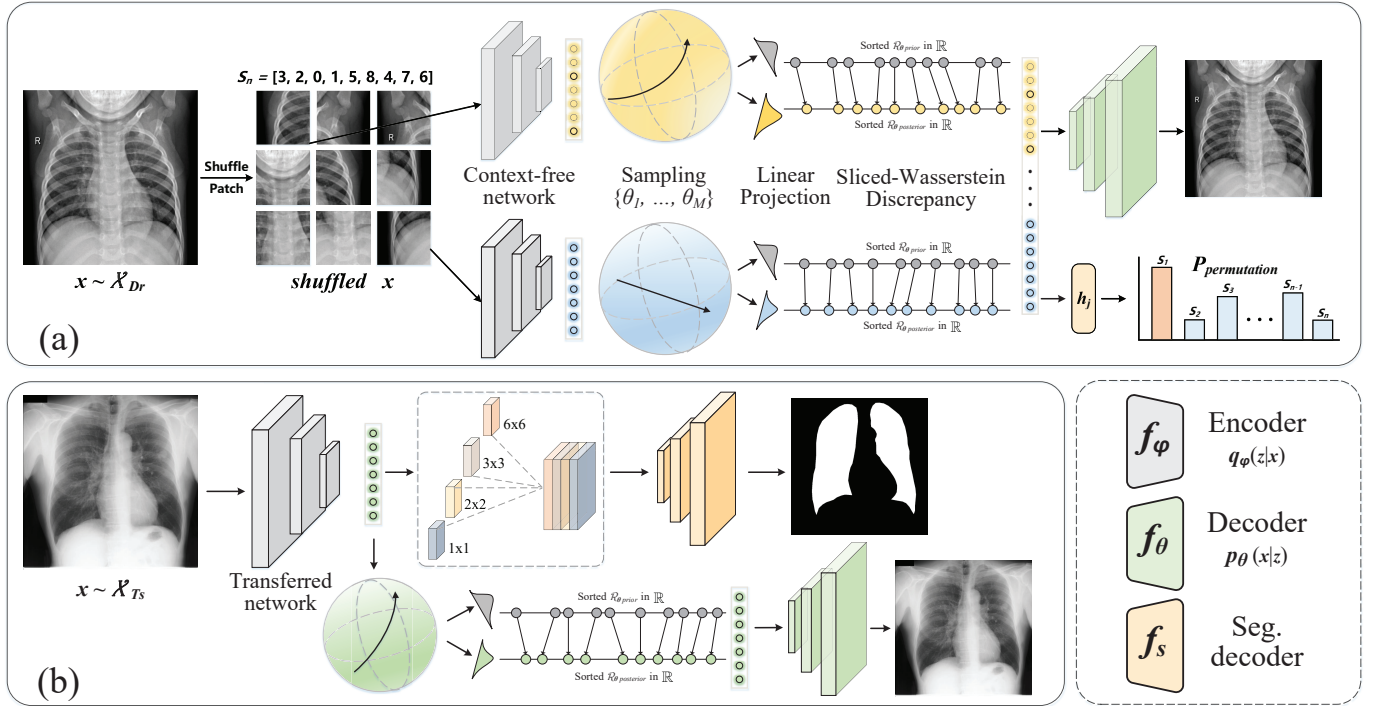


Fig. 2: Illustration of our proposed method segmentation framework, which consists of two main phases: (a) pretraining the T-AE network on domain-related (Dr) data; (b) finetuning the downstream PSPNet-based segmentation network.

is divided into two part: a feature mapping function $f_\phi(\cdot) : \mathcal{X}_{Dr} \rightarrow \mathcal{Z}$ and a probability estimation function $f_\theta(\cdot) : \mathcal{Z} \rightarrow \mathcal{X}_{Dr}$. One common strategy is that train $f_\phi(\cdot)$ and $f_\theta(\cdot)$ to reconstruct the input.

B. Tile-wise Autoencoder for Pretraining

As we pointed out before and empirically analysis in the experiments section, pretraining (especially pretraining on domain-related data) is important for robust generalized medical image segmentation algorithms. In this paper, we propose a tile-wise autoencoder pretraining method, under the unsupervised learning setting. The motivation is that although generative models are good at learning discriminative and useful features, the vanilla autoencoder is too simple to capture the transferable representations and VAEs [39] are hampered by the over-regularization and collapsed features.

Here, we focus on the variational inference-based generative model and alleviate its innate challenges, furthermore, make it suitable for the domain pretraining. VAEs [39] include two main part: an inference network (i.e., encoder) $f_\phi(\cdot)$ for modeling the posterior distribution $q_\phi(z|x)$ and a generative network (or decoder) $f_\theta(\cdot)$ fitted $p_\theta(x|z)$. It can be used to estimate the true underlying distribution $p_{Dr}(x)$. The parametric inference and generative neural network can be trained jointly via maximum marginal log-likelihood $\log p_{Dr}(x)$, which equals to maximizing the evidence lower bound (ELBO) with introducing an amortized distribution $q_\phi(z|x)$:

$$\begin{aligned} \log p_\theta(x) &\geq \mathbb{E}_{q_\phi(z|x)}[\log p_\theta(x|z)] - D_{KL}(q_\phi(z|x) \parallel p(z)) \\ &:= \mathcal{L}_{ELBO}(x; \theta, \phi). \end{aligned} \quad (1)$$

As discussed in previous works [42] [43], one limitation of VAEs is that the collapsed feature causes the over-blurry reconstruction. Analyzed theoretically, the simplistic prior distribution $p(z)$ (such as Gaussian distribution) is far to generate diverse data. In addition, Kullback–Leibler (KL) divergence is used for approximating the inference distribution $q_\phi(z|x)$ to the prior distribution $p(z)$ in most existing VAEs-based methods. However, it is a strong notion of distance that the fraction in log operator usually takes the large gradient [42]. Therefore, minimizing KL divergence without constraints could make the latent feature over-fit the prior distribution and carry less information about the input.

For mitigating the above problems in the pretraining task, we propose a novel Tile-wise autoencoder (T-AE) architecture, as shown in Fig. 2. In particular, we separate the image into a regular $n \times n$ grid of tiles $x_M = \{x_M^1, \dots, x_M^M, \dots, x_M^{n^2}\}$. Each patch is assigned a prior distribution $p(z^k)$, therefore, we transform the approximating the whole image with one prior into approximating the whole image with n^2 priors. This is an effective yet simple technique to address the limited capability of the simplistic prior. Moreover, for alleviating the over-regularization caused by the strong notion (i.e. KL divergence), we introduce the sliced-Wasserstein distance to measure the distance between the inference posterior distribution $q_\phi(z^k|x^k)$ and its prior $p(z^k)$. Based on but different from the p-Wasserstein distance

$$W_p(p_X, p_Y) = \inf_{\gamma \in \Pi(p_X, p_Y)} \mathbb{E}_{(X, Y) \sim \gamma} [d^p(X, Y)]^{\frac{1}{p}}, \quad (2)$$

where $\Pi(p_X, p_Y)$ means the family of all joint distributions (i.e., transport maps in the optimal transport), and d is a metric function, such as the Euclidean distance $d(x, y) = \|x - y\|^2$,

the sliced-Wasserstein distance avoids high computational cost while maintains the topology characteristic. It has been effectively utilized in the generative models [43]. Here, we integrate the sliced-Wasserstein distance to replace the KL divergence in the variational autoencoders:

$$\mathcal{L}_{SW} = \sum_k \frac{n^2}{|\Theta|^k} \sum_{\vartheta \in \Theta^k} W_p(\mathcal{R}_{q_{\varphi}(z^k|x^k)}(\cdot; \vartheta), \mathcal{R}_{p(z^k)}(\cdot; \vartheta)), \quad (3)$$

where Θ denotes the set of the d -dimensional unit sphere \mathbb{S}^{d-1} , $p(z^k)$ can be assigned as the Gaussian distribution $\mathcal{N}(\mu^k, \sigma^2)$, and the \mathcal{R} is the radon transform (linear slicing) marginal distribution.

Moreover, motivated by the philosophy of *jigsaw puzzles* that the pretext to help children learn geography [21], we introduce the solving *jigsaw puzzles* pretext in our proposed method. Especially, beginning with $n \times n$ grid of tiles $x_M = \{x_M^1, \dots, x_M^k, \dots, x_M^{n^2}\}$, we shuffle them according to the pseudo permutation label S_i . Following [21], each tile is sent to the context-free network, which can be implemented with a Siamese-wise encoder $f_{\varphi}(\cdot)$. In the end, the accumulated features of all patches are optimized to re-order the image. In other words, the latent codes of the whole image are capable to predict the permutation label S_i :

$$\mathcal{L}_p = - \sum_i^N p(S_i) \log p(\hat{S}_i|z_M), \quad (4)$$

where $z_M = \{z_M^1, \dots, z_M^k, \dots, z_M^{n^2}\}$ represents the accumulated tile features. Training the re-order objective endows the generative model with both local and global structure perception capability, which can improve learning meaningful representations in the pretraining phase.

In conclusion, coupling with the reconstruction objective \mathcal{L}_{AE} , such as mean squared error (MSE), the proposed pre-training method (T-AE) is trained with

$$\mathcal{L}_{T-AE} = \mathcal{L}_{AE} + \mathcal{L}_{SW} + \mathcal{L}_p \quad (5)$$

to learn transferable and useful representations. Note that our proposed pretraining technique is a label-free method, which is suitable to apply in the medical image analysis system. In addition, most the-state-of-art segmentation networks do not follow the common feature extraction backbone (e.g., ResNet-50), i.e., they tailor the architecture for their particular cases, such as the vanilla UNet [31]. Therefore, the existed pretrained model cannot be suitable. Moreover, previous pretraining methods are time-consuming, while our proposed method (T-AE) is an efficient yet simple alternative.

C. Segmentation Framework with Reconstruction

Based on the common transfer learning setting, the pre-trained model is utilized as the initiation for the target task. In this section, we provide the detail of the downstream part of our proposed robust generalized medical image segmentation framework. While the deep learning-based segmentation networks have been widely developed (such as UNet [31], PSPNet [34]), in this paper, we focus on how to further

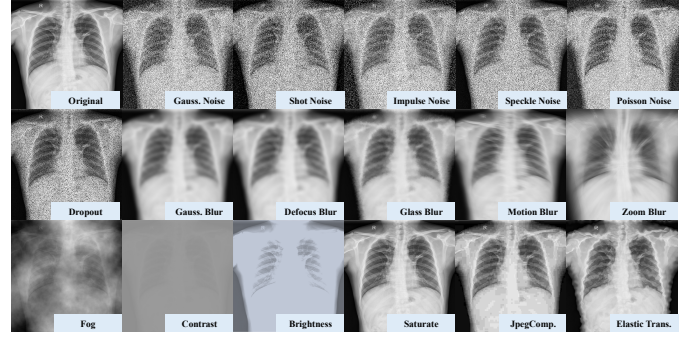


Fig. 3: The visualization of different data corruptions and perturbations. We choose these noises, blur, and digital transformations that are common in real-world applications for verification of the robustness of our model.

improve the generalization and robustness of these architecture. Including but not limited to PSPNet and UNet, we introduce a reconstruction task incorporated with the primary task (segmentation the lung). The designed auxiliary task does not conflict with the primary task, meanwhile, it encourages the learned high-level features can be decoded, which can regularize the learned representation especially when the dataset size is limited. In particular, unlike the winner of the BraTS challenge [44] that adds variational autoencoder (VAE) branch, our segmentation network integrates the sliced-Wasserstein autoencoder (SWAE) followed our proposed pre-training methods (T-AE). As discussed in the previous section, sliced-Wasserstein is a weaker notion distance compared with KL divergence of VAE. The weaker regularization is more appropriate for the auxiliary task.

Formally, given the target domain dataset T_S including N cases, in most cases, with a limited size N , we construct a segmentation branch and a SWAE branch. The segmentation branch consists of an encoder $f_{\varphi}(\cdot)$ and a segmentation decoder $f_s(\cdot)$. The SWAE branch is made up primarily of a shared encoder $f_{\varphi}(\cdot)$ and a reconstruction decoder $f_{\theta}(\cdot)$. The shared encoder $f_{\varphi}(\cdot)$ is initialized from the pretrained model then are finetuned with T_S . The weight of $f_s(\cdot)$ is training from scratch with segmentation loss, and the weight of $f_{\theta}(\cdot)$ is transferred from the pretrained model then finetuned.

After initializing the weight from our proposed pretrained method, the segmentation network is optimized with:

$$\mathcal{L}_{seg} = \mathcal{L}_{Dice} + \mathcal{L}_{AE} + \mathcal{L}_{SW}, \quad (6)$$

where \mathcal{L}_{AE} and \mathcal{L}_{SW} is same as Eq. 5, and \mathcal{L}_{Dice} is a soft dice loss function [45] calculated with the segmentation decoder predict \hat{y}_N and the mask y_N .

In summary, our proposed robust generalized medical image segmentation framework consists of two stages: pretraining on the unlabeled domain-related dataset D_r with T-AE network to learn the general and meaningful representations; finetuning on the target domain dataset T_s . This transfer learning framework improves the model generalization and robustness, such as the data data corruptions and perturbations in Fig. 3.

IV. EXPERIMENTS

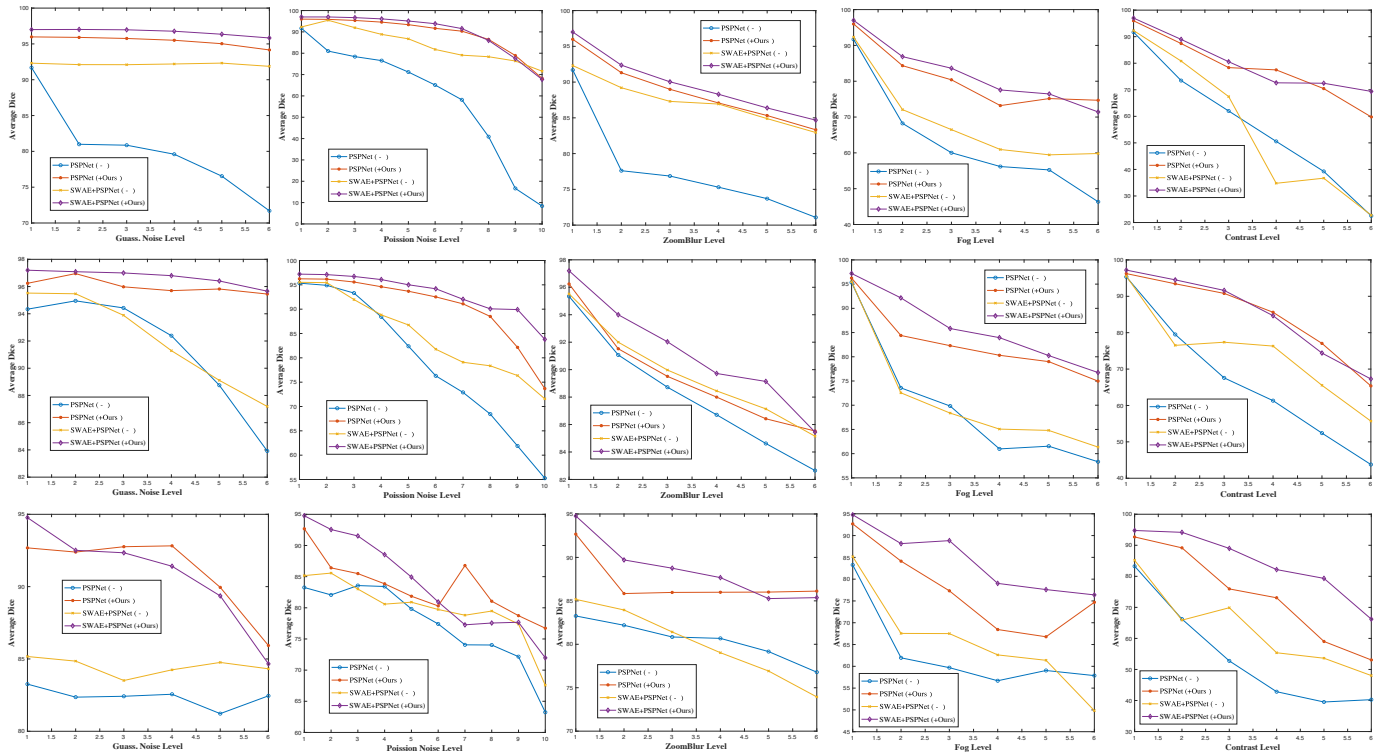


Fig. 4: The robustness performance comparison between our proposed method and baselines on different data corruption. The experiments conducted on the MC dataset are reported in the first row; on the JSRT dataset are reported in the second row; the results on the SH dataset are shown in the third row.

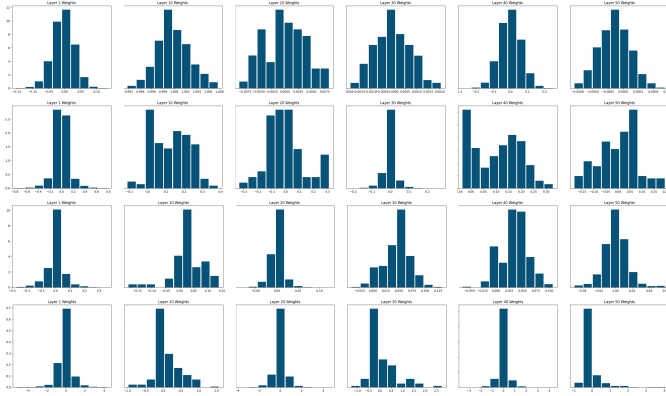


Fig. 5: The visualization of the network's weights distribution. Each column denotes one layer weights. The first row shows weights of ResNet-50 trained from scratch; the second row is with the ImageNet pretrained model; the third one is with the MoCo; the last row denotes utilizing our T-AE.

A. Datasets

Pretraining: The pretraining dataset for our proposed method (T-AE) should be related or the same to the target domain. In this paper, considering the segmentation lung on the chest X-ray image, we also utilize the chest X-ray (anterior-posterior) dataset for pretraining. The dataset [46] includes a total of 5,232 chest X-ray images, which consists of 1,349 normal cases, 3,883 characterized as depicting pneumonia. Here, we only use the 1,349 normal samples to construct the

domain-related pretraining dataset D_r .

Target Domain: Our designed medical image segmentation framework is conducted on **three** chest X-ray (anterior-posterior) datasets: Montgomery County chest X-ray set (MC) [47], Japanese Society of Radiological Technology database (JSRT) [48], and Shenzhen chest X-ray set (SH) [47]. In particular, the MC dataset contains 138 posterior-anterior x-rays. The size of the image is either 4,020 by 4,892 or 4,892 by 4,020 pixels. Furthermore, the annotated lung binary masks are provided in the dataset. The JSRT database is a publicly available dataset with 247 anterior-posterior chest X-ray gray images. The X-rays are scanned from films to a size of 2048x2048 pixels. In each image, the lung fields have been manually segmented to provide a reference standard. SH X-ray set includes a total of 662 x-rays showing manifestations of TB. The size varies but is approximately $3K \times 3K$ pixels. The lung masks are not provided in the database, but were prepared manually by National Technical University of Ukraine¹.

B. Experiment Setup

Implementation details: For T-AE pretraining, given the domain-related dataset during training, we first define the grid size ($n \times n$) to separate the image as tiles and the permutation pseudo-label subset S . Following the work [21], we split an image into 3 by 3 tiles then shuffle them according to a random permutation. Each tile is sent to the Siamese-network $f_\phi(\cdot)$, in parallel. The $f_\phi(\cdot)$ is implemented with the backbone

¹<https://www.kaggle.com/yoctoman/shcxr-lung-mask>

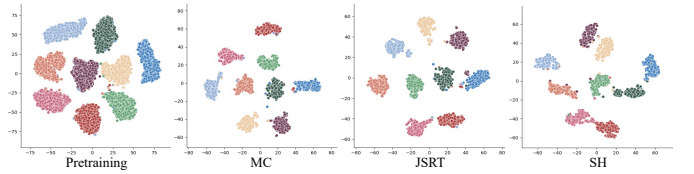
TABLE I: Comparison robustness performances among different data corruption in the lung segmentation task on MC dataset using PSPNet [34] as baseline. Dice is utilized as the evaluation metric.

Corruption	PSPNet (—)	PSPNet (+VAE)	PSPNet (+ImageNet)	PSPNet (+Jigsaw)	PSPNet (+MoCo)	PSPNet (+Ours)	SWAE-PSPNet (—)	SWAE-PSPNet (+MoCo)	SWAE-PSPNet (+Ours)
Ori.	91.69 ± 0.1 —	95.73 ± 0.3 —	96.02 ± 0.3 —	96.03 ± 0.2 —	97.27 ± 0.2 —	95.98 ± 0.1 —	92.31 ± 0.2 —	97.04 ± 0.1 —	96.95 ± 0.2 —
Gauss. Noise	82.24 ± 0.3 ↓	83.41 ± 0.4 ↓	75.82 ± 0.2 ↓	73.29 ± 0.2 ↓	82.01 ± 0.4 ↓	94.14 ± 0.2 ↓	92.01 ± 0.3 ↓	88.78 ± 0.2 ↓	95.80 ± 0.3 ↓
Shot Noise	82.22 ± 0.3 ↓	69.53 ± 0.2 ↓	86.93 ± 0.2 ↓	85.75 ± 0.2 ↓	87.53 ± 0.1 ↓	94.19 ± 0.3 ↓	90.68 ± 0.2 ↓	89.53 ± 0.1 ↓	95.75 ± 0.1 ↓
Impulse Noise	72.48 ± 0.3 ↓	78.20 ± 0.1 ↓	72.63 ± 0.3 ↓	88.30 ± 0.2 ↓	78.90 ± 0.2 ↓	94.41 ± 0.1 ↓	92.19 ± 0.1 ↓	90.07 ± 0.2 ↓	95.83 ± 0.2 ↓
Speckle Noise	82.28 ± 0.2 ↓	84.81 ± 0.3 ↓	79.96 ± 0.1 ↓	72.78 ± 0.1 ↓	85.79 ± 0.2 ↓	94.02 ± 0.1 ↓	90.48 ± 0.1 ↓	91.03 ± 0.1 ↓	95.96 ± 0.2 ↓
Poisson Noise	71.18 ± 0.4 ↓	75.94 ± 0.1 ↓	78.96 ± 0.2 ↓	79.71 ± 0.1 ↓	86.20 ± 0.2 ↓	93.29 ± 0.3 ↓	91.24 ± 0.4 ↓	89.06 ± 0.2 ↓	95.06 ± 0.3 ↓
Dropout	82.60 ± 0.3 ↓	79.93 ± 0.3 ↓	78.50 ± 0.2 ↓	73.88 ± 0.4 ↓	86.56 ± 0.1 ↓	92.65 ± 0.3 ↓	90.55 ± 0.4 ↓	95.54 ± 0.1 ↓	95.33 ± 0.2 ↓
Gauss. Blur	80.10 ± 0.3 ↓	94.36 ± 0.4 ↓	85.99 ± 0.4 ↓	78.85 ± 0.1 ↓	76.19 ± 0.1 ↓	94.96 ± 0.4 ↓	91.59 ± 0.3 ↓	94.69 ± 0.1 ↓	96.25 ± 0.1 ↓
Glass Blur	82.19 ± 0.2 ↓	94.38 ± 0.1 ↓	83.39 ± 0.2 ↓	88.74 ± 0.4 ↓	90.75 ± 0.2 ↓	94.97 ± 0.2 ↓	92.17 ± 0.3 ↓	95.58 ± 0.1 ↓	96.03 ± 0.1 ↓
Defocus Blur	80.14 ± 0.1 ↓	94.54 ± 0.3 ↓	86.49 ± 0.3 ↓	80.63 ± 0.2 ↓	85.60 ± 0.2 ↓	95.07 ± 0.2 ↓	91.98 ± 0.3 ↓	92.75 ± 0.1 ↓	96.34 ± 0.2 ↓
Motion Blur	78.24 ± 0.3 ↓	88.39 ± 0.2 ↓	83.52 ± 0.1 ↓	85.22 ± 0.2 ↓	91.02 ± 0.4 ↓	89.48 ± 0.1 ↓	87.06 ± 0.3 ↓	89.34 ± 0.2 ↓	90.71 ± 0.3 ↓
Zoom Blur	76.68 ± 0.2 ↓	78.18 ± 0.3 ↓	85.07 ± 0.2 ↓	83.74 ± 0.3 ↓	88.41 ± 0.1 ↓	82.02 ± 0.1 ↓	82.95 ± 0.3 ↓	88.89 ± 0.1 ↓	84.68 ± 0.2 ↓
Fog	46.58 ± 0.3 ↓	51.37 ± 0.2 ↓	70.02 ± 0.2 ↓	70.89 ± 0.3 ↓	75.43 ± 0.1 ↓	67.74 ± 0.2 ↓	58.34 ± 0.2 ↓	76.55 ± 0.2 ↓	71.19 ± 0.2 ↓
Contrast	22.49 ± 0.4 ↓	49.04 ± 0.2 ↓	31.05 ± 0.2 ↓	41.39 ± 0.3 ↓	56.25 ± 0.2 ↓	47.78 ± 0.2 ↓	22.17 ± 0.3 ↓	57.66 ± 0.2 ↓	59.38 ± 0.1 ↓
Brightness	47.48 ± 0.2 ↓	72.33 ± 0.1 ↓	89.89 ± 0.2 ↓	87.94 ± 0.1 ↓	82.16 ± 0.2 ↓	75.62 ± 0.2 ↓	64.40 ± 0.3 ↓	91.50 ± 0.3 ↓	97.09 ± 0.2 ↑
Saturate	83.16 ± 0.2 ↓	95.73 ± 0.2 —	96.13 ± 0.2 ↑	96.03 ± 0.1 —	97.28 ± 0.1 ↑	95.98 ± 0.3 —	92.38 ± 0.3 ↓	97.43 ± 0.1 ↑	97.09 ± 0.2 ↓
JpegComp.	83.05 ± 0.2 ↓	95.75 ± 0.3 ↓	89.24 ± 0.3 ↓	90.86 ± 0.1 ↓	92.48 ± 0.1 ↓	95.80 ± 0.5 ↓	92.23 ± 0.3 ↓	92.36 ± 0.2 ↓	96.93 ± 0.4 ↓
Elastic Trans.	82.82 ± 0.4 ↓	95.17 ± 0.1 ↓	93.36 ± 0.4 ↓	93.20 ± 0.3 ↓	96.43 ± 0.5 ↓	95.60 ± 0.3 ↓	92.62 ± 0.1 ↑	94.16 ± 0.2 ↓	96.72 ± 0.2 ↓
Avg.	72.63 ↓ (18.46)	81.24 ↓ (14.49)	80.41 ↓ (15.61)	80.66 ↓ (15.37)	84.65 ↓ (12.62)	88.10 ↓ (7.88)	83.24 ↓ (9.07)	89.11 ↓ (7.93)	91.18 ↓ (5.77)

TABLE II: Comparison robustness performances among different data corruption in the lung segmentation task on MC dataset using UNet [31] as baseline. Dice is utilized as the evaluation metric.

Corruption	UNet (—)	UNet (+ VAE)	UNet (+Ours)	SWAE-UNet (—)	SWAE-UNet (+Ours)
Ori.	89.95 ± 0.3 —	92.80 ± 0.3 —	95.35 ± 0.2 —	92.97 ± 0.3 —	95.89 ± 0.1 —
Gauss. Noise	71.32 ± 0.2 ↓	90.87 ± 0.3 ↓	89.66 ± 0.2 ↓	81.67 ± 0.1 ↓	93.47 ± 0.2 ↓
Shot Noise	86.86 ± 0.1 ↓	89.04 ± 0.2 ↓	94.20 ± 0.2 ↓	86.82 ± 0.2 ↓	94.33 ± 0.3 ↓
Impulse Noise	69.00 ± 0.3 ↓	90.23 ± 0.2 ↓	93.95 ± 0.2 ↓	78.13 ± 0.4 ↓	93.40 ± 0.2 ↓
Speckle Noise	88.39 ± 0.2 ↓	90.45 ± 0.4 ↓	94.17 ± 0.4 ↓	87.72 ± 0.2 ↓	94.78 ± 0.1 ↓
Poisson Noise	71.66 ± 0.4 ↓	89.94 ± 0.2 ↓	90.94 ± 0.4 ↓	75.54 ± 0.2 ↓	87.23 ± 0.4 ↓
Dropout	87.62 ± 0.3 ↓	92.31 ± 0.1 ↓	93.24 ± 0.2 ↓	89.81 ± 0.1 ↓	94.10 ± 0.1 ↓
Gauss. Blur	90.44 ± 0.4 ↓	89.08 ± 0.4 ↓	94.83 ± 0.2 ↓	84.39 ± 0.3 ↓	95.55 ± 0.3 ↓
Glass Blur	88.45 ± 0.3 ↓	89.81 ± 0.2 ↓	94.45 ± 0.3 ↓	91.92 ± 0.3 ↓	95.28 ± 0.4 ↓
Defocus Blur	89.79 ± 0.3 ↓	89.56 ± 0.3 ↓	94.75 ± 0.3 ↑	88.35 ± 0.2 ↓	95.25 ± 0.5 ↓
Motion Blur	86.62 ± 0.3 ↓	87.53 ± 0.1 ↓	90.17 ± 0.5 ↓	84.31 ± 0.3 ↓	90.10 ± 0.2 ↓
Zoom Blur	82.97 ± 0.4 ↓	81.37 ± 0.2 ↓	83.16 ± 0.2 ↓	86.68 ± 0.2 ↓	82.30 ± 0.2 ↓
Fog	35.90 ± 0.5 ↓	59.76 ± 0.3 ↓	59.47 ± 0.1 ↓	61.08 ± 0.3 ↓	61.74 ± 0.3 ↓
Contrast	25.11 ± 0.5 ↓	20.45 ± 0.2 ↓	58.52 ± 0.1 ↓	23.42 ± 0.4 ↓	63.50 ± 0.2 ↓
Brightness	00.98 ± 0.6 ↓	70.75 ± 0.4 ↓	56.32 ± 0.3 ↓	16.69 ± 0.3 ↓	71.84 ± 0.2 ↓
Saturate	90.44 ± 0.4 ↑	91.14 ± 0.1 ↓	94.19 ± 0.1 ↓	89.48 ± 0.2 ↓	94.67 ± 0.3 ↓
JpegComp.	88.21 ± 0.2 ↓	89.93 ± 0.4 ↓	94.64 ± 0.1 ↓	85.97 ± 0.3 ↓	95.89 ± 0.4 ↓
Elastic Trans.	89.52 ± 0.2 ↓	88.65 ± 0.2 ↓	94.68 ± 0.3 ↑	89.39 ± 0.2 ↓	95.95 ± 0.1 ↓
Avg.	73.11 ↓ (16.84)	82.40 ↓ (10.40)	86.55 ↓ (8.80)	76.52 ↓ (16.45)	88.20 ↓ (7.69)

of the UNet [31] or the standard ResNet-50 network of the PSPNet [34]. For each tile latent feature z_M^k , we assign a Gaussian distribution $\mathcal{N}(k, 1)$ as the prior distribution for approximating, respectively. All tiles latent features are then combined before reassembling by the flow-based warp. The auxiliary solving *jigsaw puzzle* network h_j includes one fully-connected (FC) layer to predict the permutation label. The decoder $f_\theta(\cdot)$ consists of multiple convolutional layer blocks, which include Upsample-Conv-BN-ReLU layers. We resize the input image to 624×624 . The reconstruction loss function is the mean squared error (MSE), and the objective of *jigsaw puzzle* is the cross-entropy. The stochastic gradient descent (SGD) with an initial learning rate of 0.01 is used for the

**Fig. 6:** T-SNE visualization for the latent distribution of pretrained T-AE. Each color denotes a tile class.

T-AE pretraining model ².

For the downstream segmentation part, we choose two representative segmentation networks (PSPNet and UNet). The auxiliary reconstruction branch is constructed with the same architecture of T-AE. The input images are resized to 624×624 . The reconstruction error is the mean squared error (MSE), and the segmentation objective is the dice loss function. The SGD with an initial learning rate of 0.001 is used to finetune the segmentation network. All experiments are conducted on Pytorch library with a NVIDIA GeForce GTX 3080 GPU.

C. Robustness Results

Visualization results: Firstly, our framework robustness performances with different types of corruptions and levels are visualized in Fig. 4. The sparsity of the weight is compared in Fig. 5. A degree of sparsity can be more robust. We shows the histograms of the hidden layer's weights. Compared with training from scratch, pretrained on classification ImageNet [20], and MoCo [27], weights are sparser with our proposed T-AE. Moreover, the robust segmentation results with three types of corruption of the MC dataset are shown in Fig. 8.

²The code is available: <https://github.com/YurongChen1998/yurong-lib>

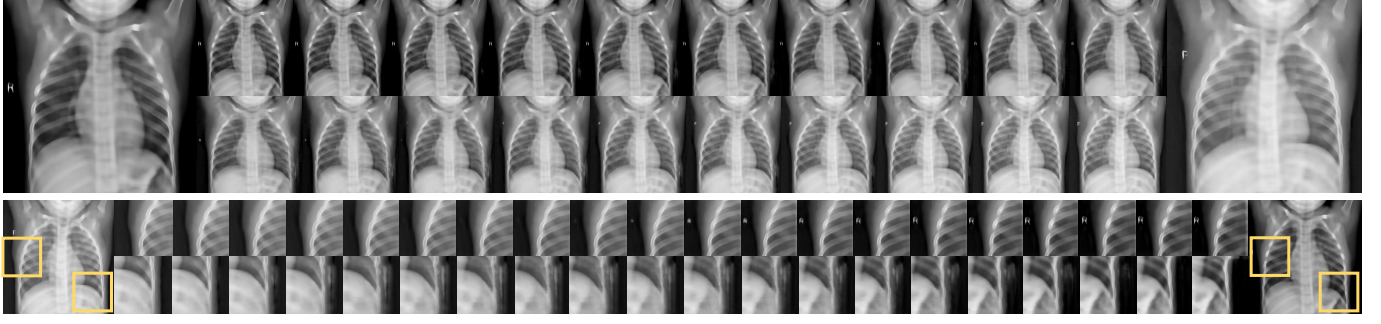


Fig. 7: Interpolations in the latent space of the trained T-AE. The first row indicates that interpolations in the whole image latent space. The last row is only linear interpolation in one patch latent space. Those interpolations are operated between two latent codes conditioned by real image inputs (the first and last column).

TABLE III: Summary of model generalization performance in the lung segmentation task on MC, JSRT, SH X-ray datasets (abbreviate M, J, and S for simple). Dice is utilized as the evaluation metric.

Method	Dataset	M → M	M → J	M → S	J → J	J → M	J → S	S → S	S → M	S → J	Avg.
Rashid <i>et al.</i> [36]		95.40	/	/	95.10	/	/	/	/	/	/
Candemir <i>et al.</i> [37]		96.10 ± 0.8	/	/	96.70 ± 1.8	/	/	/	/	/	/
DEFU-Net [32]		95.78 –	91.54 ↓	/	/	/	96.67 –	92.27 ↓	/	/	/
DeepLab V3+ [33]		87.04 ± 0.3 –	85.26 ± 0.2 ↓	70.51 ± 0.5 ↓	91.42 ± 0.1 –	92.52 ± 0.2 ↑	89.73 ± 0.3 ↓	86.49 ± 0.2 –	20.45 ± 0.6 ↓	61.24 ± 0.4	76.07
UNet [31]		89.95 ± 0.1 –	73.20 ± 0.2 ↓	77.74 ± 0.2 ↓	94.18 ± 0.3 –	82.74 ± 0.4 ↓	85.71 ± 0.2 ↓	88.03 ± 0.6 –	46.69 ± 0.3 ↓	72.24 ± 0.5 ↓	78.94
UNet (+VAE)		92.80 ± 0.2 –	89.15 ± 0.3 ↓	80.19 ± 0.2 ↓	95.43 ± 0.3 –	84.42 ± 0.3 ↓	90.75 ± 0.1 ↓	86.66 ± 0.2 –	83.69 ± 0.2 ↓	83.38 ± 0.3 ↓	87.39
UNet (+Ours)		94.35 ± 0.4 –	92.38 ± 0.1 ↓	86.05 ± 0.3 ↓	94.41 ± 0.2 –	84.58 ± 0.2 ↓	89.53 ± 0.3 ↓	91.31 ± 0.3 –	90.83 ± 0.1 ↓	88.44 ± 0.2 ↓	90.21
SWAE-UNet		92.87 ± 0.3 –	82.52 ± 0.1 ↓	75.26 ± 0.3 ↓	95.07 ± 0.2 –	91.19 ± 0.1 ↓	89.43 ± 0.4 ↓	89.34 ± 0.3 –	78.26 ± 0.4 ↓	82.51 ± 0.1 ↓	88.55
SWAE-UNet (+Ours)		95.98 ± 0.1 –	94.87 ± 0.1 ↓	91.65 ± 0.3 ↓	96.56 ± 0.4 –	95.86 ± 0.1 ↓	96.00 ± 0.2 ↓	93.17 ± 0.6 –	89.48 ± 0.2 ↓	90.35 ± 0.3 ↓	93.78
PSPNet [34]		91.69 ± 0.2 –	84.49 ± 0.1 ↓	63.84 ± 0.3 ↓	95.34 ± 0.2 –	83.40 ± 0.5 ↓	85.45 ± 0.3 ↓	83.26 ± 0.4 –	29.52 ± 0.3 ↓	76.61 ± 0.2 ↓	77.07
PSPNet (+SwAV)		95.65 ± 0.3 –	92.18 ± 0.1 ↓	90.97 ± 0.6 ↓	95.80 ± 0.2 –	94.33 ± 0.5 ↓	71.43 ± 0.2 ↓	91.34 ± 0.1 –	60.97 ± 0.3 ↓	67.83 ± 0.2 ↓	84.72
PSPNet (+Color.)		91.94 ± 0.1 –	85.97 ± 0.3 ↓	85.03 ± 0.2 ↓	94.25 ± 0.3 –	92.48 ± 0.2 ↓	88.63 ± 0.4 ↓	86.63 ± 0.6 –	85.23 ± 0.1 ↓	79.93 ± 0.4 ↓	87.79
PSPNet (+VAE)		95.73 ± 0.2 –	92.98 ± 0.1 ↓	84.87 ± 0.3 ↓	94.26 ± 0.1 –	89.00 ± 0.3 ↓	87.56 ± 0.2 ↓	91.97 ± 0.3 –	78.53 ± 0.2 ↓	86.86 ± 0.3 ↓	89.08
PSPNet (+BYOL)		94.75 ± 0.1 –	92.41 ± 0.4 ↓	91.41 ± 0.2 ↓	95.37 ± 0.3 –	93.86 ± 0.2 ↓	92.61 ± 0.1 ↓	92.32 ± 0.4 –	90.26 ± 0.5 ↓	90.51 ± 0.2 ↓	92.61
PSPNet (+RotNet)		95.94 ± 0.2 –	93.98 ± 0.1 ↓	92.19 ± 0.2 ↓	96.20 ± 0.4 –	93.41 ± 0.1 ↓	92.43 ± 0.4 ↓	93.00 ± 0.5 –	91.06 ± 0.2 ↓	89.16 ± 0.3 ↓	93.04
PSPNet (+SimCLR)		95.62 ± 0.3 –	92.92 ± 0.1 ↓	92.72 ± 0.5 ↓	95.88 ± 0.1 –	94.55 ± 0.4 ↓	94.04 ± 0.2 ↓	93.29 ± 0.3 –	90.74 ± 0.2 ↓	91.48 ± 0.1 ↓	93.47
PSPNet (+ImageNet)		96.02 ± 0.1 –	94.40 ± 0.5 ↓	94.56 ± 0.2 ↓	96.54 ± 0.3 –	95.26 ± 0.2 ↓	94.24 ± 0.2 ↓	92.67 ± 0.3 –	91.07 ± 0.1 ↓	90.89 ± 0.3 ↓	93.96
PSPNet (+Jigsaw)		96.02 ± 0.3 –	94.38 ± 0.3 ↓	93.26 ± 0.1 ↓	96.32 ± 0.3 –	93.79 ± 0.2 ↓	93.99 ± 0.2 ↓	93.95 ± 0.1 –	92.33 ± 0.1 ↓	92.81 ± 0.5 ↓	94.09
PSPNet (+MoCo)		97.27 ± 0.1 –	95.01 ± 0.1 ↓	94.71 ± 0.4 ↓	96.50 ± 0.2 –	95.61 ± 0.3 ↓	94.49 ± 0.3 ↓	94.75 ± 0.3 –	93.22 ± 0.2 ↓	92.47 ± 0.1 ↓	95.00
PSPNet (+Ours)		95.98 ± 0.2 –	93.90 ± 0.3 ↓	90.92 ± 0.1 ↓	96.24 ± 0.5 –	93.80 ± 0.1 ↓	92.15 ± 0.2 ↓	92.68 ± 0.1 –	90.61 ± 0.5 ↓	89.67 ± 0.3 ↓	92.88
SWAE-PSPNet		92.31 ± 0.1 –	88.86 ± 0.3 ↓	72.66 ± 0.1 ↓	95.51 ± 0.6 –	86.02 ± 0.4 ↓	84.60 ± 0.2 ↓	85.17 ± 0.5 –	56.60 ± 0.2 ↓	71.87 ± 0.3 ↓	81.51
SWAE-PSPNet (+MoCo)		97.04 ± 0.2 –	95.56 ± 0.1 ↓	94.63 ± 0.2 ↓	96.80 ± 0.1 –	96.30 ± 0.2 ↓	94.53 ± 0.2 ↓	94.80 ± 0.2 –	94.68 ± 0.1 ↑	90.10 ± 0.2 ↓	94.94
SWAE-PSPNet (+Ours)		96.95 ± 0.3 –	95.69 ± 0.2 ↓	95.05 ± 0.2 ↓	97.19 ± 0.1 –	96.23 ± 0.1 ↓	95.02 ± 0.2 ↓	94.77 ± 0.1 –	92.45 ± 0.2 ↓	92.82 ± 0.3 ↓	95.13

TABLE IV: Summary of model generalization performance in the lung segmentation task under the few-shot learning condition on MC, JSRT, SH X-ray datasets (abbreviate M, J, and S for simple). Dice is utilized as the evaluation metric.

Method	Dataset	M → M	M → J	M → S	J → J	J → M	J → S	S → S	S → M	S → J	Avg.
Labeled 2%	PSPNet [34]	65.24 ± 0.3 –	55.93 ± 0.2 ↓	37.51 ± 0.2 ↓	71.07 ± 0.2 –	57.28 ± 0.3 ↓	49.53 ± 0.1 ↓	61.94 ± 0.3 –	25.26 ± 0.3 ↓	52.90 ± 0.2 ↓	52.96
	PSPNet (+Ours)	75.12 ± 0.1 –	80.25 ± 0.1 ↑	70.78 ± 0.2 ↓	81.90 ± 0.2 –	75.01 ± 0.2 ↓	73.33 ± 0.1 ↓	68.54 ± 0.1 –	70.26 ± 0.2 ↑	72.64 ± 0.1 ↑	74.20
	SWAE-PSPNet (—)	68.56 ± 0.1 –	71.03 ± 0.1 ↑	61.05 ± 0.2 ↓	69.14 ± 0.3 –	61.14 ± 0.2 ↓	63.76 ± 0.2 ↓	60.42 ± 0.1 –	40.39 ± 0.3 ↓	56.74 ± 0.3 ↓	61.36
	SWAE-PSPNet (+Ours)	75.90 ± 0.1 –	80.39 ± 0.2 ↑	73.57 ± 0.2 ↓	83.28 ± 0.1 –	74.06 ± 0.2 ↓	76.70 ± 0.1 ↓	90.26 ± 0.2 –	88.39 ± 0.2 ↓	88.87 ± 0.1 ↓	81.27
Labeled 5%	PSPNet [34]	73.75 ± 0.2 –	74.71 ± 0.2 ↑	56.82 ± 0.3 ↓	74.02 ± 0.2 –	64.06 ± 0.3 ↓	59.41 ± 0.2 ↓	63.84 ± 0.2 –	28.39 ± 0.3 ↓	58.80 ± 0.2 ↓	61.53
	PSPNet (+Ours)	81.78 ± 0.2 –	84.77 ± 0.3 ↑	74.26 ± 0.3 ↓	84.83 ± 0.2 –	76.77 ± 0.1 ↓	72.34 ± 0.2 ↓	72.34 ± 0.2 –	53.72 ± 0.3 ↓	73.40 ± 0.3 ↑	75.55
	SWAE-PSPNet (—)	76.26 ± 0.1 –	70.58 ± 0.2 ↓	64.52 ± 0.2 ↓	76.82 ± 0.2 –	66.70 ± 0.3 ↓	72.37 ± 0.3 ↓	71.55 ± 0.2 –	48.45 ± 0.2 ↓	66.74 ± 0.1 ↓	68.22
	SWAE-PSPNet (+Ours)	82.91 ± 0.1 –	84.73 ± 0.1 ↑	79.58 ± 0.2 ↓	85.64 ± 0.2 –	79.30 ± 0.1 ↑	80.52 ± 0.1 ↓	90.04 ± 0.1 –	88.10 ± 0.1 ↓	88.01 ± 0.1 ↓	84.31
Labeled 7%	PSPNet [34]	77.58 ± 0.2 –	76.28 ± 0.3 ↓	59.43 ± 0.1 ↓	81.83 ± 0.3 –	66.87 ± 0.3 ↓	75.20 ± 0.2 ↓	81.83 ± 0.3 –	32.49 ± 0.2 ↓	61.86 ± 0.2 ↓	68.15
	PSPNet (+Ours)	84.72 ± 0.2 –	84.75 ± 0.1 ↑	74.73 ± 0.2 ↓	88.70 ± 0.1 –	81.88 ± 0.1 ↓	82.78 ± 0.3 ↓	73.76 ± 0.2 –	73.70 ± 0.1 ↓	71.21 ± 0.2 ↓	79.58
	SWAE-PSPNet (—)	76.69 ± 0.1 –	79.69 ± 0.2 ↑	64.72 ± 0.2 ↓	83.89 ± 0.3 –	75.13 ± 0.3 ↓	75.18 ± 0.2 ↓	91.01 ± 0.2 –	65.09 ± 0.1 ↓	90.53 ± 0.2 ↓	77.99
	SWAE-PSPNet (+Ours)	87.00 ± 0.1 –	86.43 ± 0.2 ↓	81.14 ± 0.1 ↓	89.45 ± 0.2 –	87.45 ± 0.1 ↓	84.59 ± 0.1 ↓	92.01 ± 0.1 –	91.35 ± 0.2 ↓	91.42 ± 0.1 ↓	87.87
Labeled 10%	PSPNet [34]	79.04 ± 0.3 –	71.61 ± 0.2 ↓	63.41 ± 0.1 ↓	86.03 ± 0.4 –	72.19 ± 0.2 ↓	76.62 ± 0.2 ↓	74.40 ± 0.3 –	24.63 ± 0.2 ↓	60.12 ± 0.1 ↓	67.56
	PSPNet (+Ours)	87.20 ± 0.1 –	88.51 ± 0.2 ↑	80.39 ± 0.1 ↓	91.00 ± 0.1 –	84.81 ± 0.2 ↓	84.30 ± 0.3 ↓	84.90 ± 0.3 –	86.97 ± 0.1 ↓	89.32 ± 0.3 ↓	86.01
	SWAE-PSPNet (—)	84.90 ± 0.2 –	82.83 ± 0.1 ↓	78.54 ± 0.2 ↓	89.55 ± 0.4 –	71.22 ± 0.2 ↓	78.57 ± 0.3 ↓	90.06 ± 0.2 –	60.86 ± 0.1 ↓	72.90 ± 0.3 ↓	78.83
	SWAE-PSPNet (+Ours)	87.46 ± 0.2 –	89.26 ± 0.1 ↑	82.49 ± 0.2 ↓	95.80 ± 0.2 –	91.74 ± 0.1 ↓	89.66 ± 0.1 ↓	92.43 ± 0.2 –	90.18 ± 0.2 ↓	90.37 ± 0.2 ↓	89.93

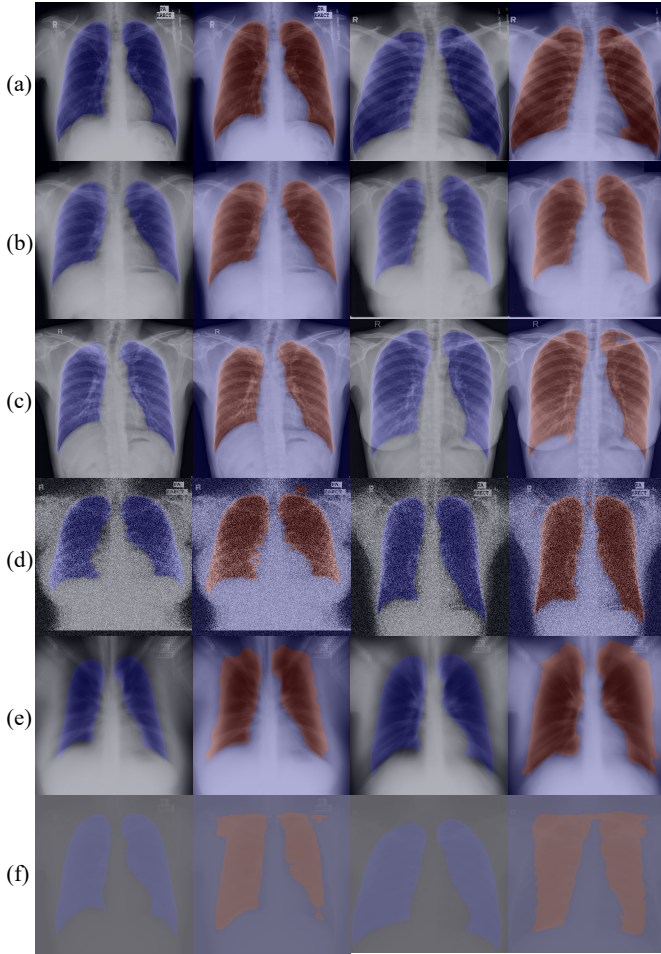


Fig. 8: The visualization of segmentation results. The blue region denotes the mask, and the red area is the predicted result. The model is trained on M dataset, then tests on (a) MC validation dataset; (b) JSRT dataset; (c) SH dataset; (d) Poisson noised MC dataset; (e) zoom blurred MC dataset; (f) contrast transformed MC dataset.

Numerical results: The robustness tests are conducted on the three target datasets with two segmentation frameworks (PSPNet and UNet). Data corruptions can be implemented with the *imgaug* library³. The results of MC datasets are shown in Table I and II. Due to the limited paper length, results of JSRT and SH datasets are reported in⁴. Compared with training from scratch or recent pretraining models, such as VAE [39], classification on ImageNet [20], Jigsaw [21], and MoCo [27], our proposed segmentation framework (SWAE-UNet or SWAE-PSPNet with T-AE pretraining) achieves the superior or comparable performance.

D. Generalization Results

Visualization results: Firstly, we visualize the latent distribution of learned representations pretrained T-AE by t-SNE in Fig. 6. We plot the distribution of the trained dataset (top-left)

and three target datasets (MC, JSRT, and SH). It's obvious that each tile clusters, which also theoretically proves that our tile-wise distribution assumption is valid. In addition, these datasets not seen in the training are also shown similar data distribution. Furthermore, the smoothness of trained T-AE latent space is shown in Fig. 7. We linearly interpolate the whole image or one patch between two inputs in the z -space. It can be seen that all latent interpolations can be decoded back to the data space, which demonstrates there is no leaky of the inference distribution. Moreover, the generalized segmentation visualization with three datasets is shown in Fig. 8.

Numerical results: The generalization tests are conducted on the three target datasets. For each experiment, we select one dataset then split it into the training set and test set. During the test phase, the trained segmentation network needs to predict its own test set and other two datasets. For example, the model trained on MC dataset is tested on MC ($M \rightarrow M$), JSRT ($M \rightarrow J$), and SH ($M \rightarrow S$) dataset, respectively. To quantitatively analyze the performance of the proposed approach, we introduce the dice coefficient as the evaluation metric [45]. The comparison between our proposed framework and several state-of-the-art segmentation methods is provided. These methods include fully CNN [36], anatomical atlases with nonrigid registration [37], DEFU-Net [32], DeepLab V3+ [33], UNet [31], and PSPNet [34]. In addition, we compare our proposed pretraining technique with SwAV [24], colorizing gray-scale images (Color.) [22], VAE [39], BYOL [25], RotNet [23], SimCLR [26], classification on ImageNet [4], Jigsaw [21], MoCo [27]. Due to the backbone of UNet is not the standard ResNet-50, we cannot load pretrained models.

The generalization performances are reported in Table III, IV. The experiment setting in Table III follows the 5-fold cross-validation, while Table IV shows results under the few-shot learning conditions. We can see that the performances of our model are consistent while others drop a lot.

E. Discussion

In the experiment section, comprehensive results demonstrate the robustness and generalization of our proposed framework. Experiments of robustness and generalization show (i) pretraining can boost the segmentation performance, furthermore, it contributes to the model robustness and generalization; (ii) utilizing the ImageNet [4] pretrained models is inferior, due to lack of domain knowledge.

V. CONCLUSION

In this paper, we propose a two-stage robust generalized medical image segmentation framework. In particular, we design a novel pretraining method (T-AE) for domain pretraining to learn meaningful representations. Then the downstream segmentation with a reconstruction branch is finetuned. Large quantities of robustness and generalization experiments demonstrate the validity of our method.

REFERENCES

- [1] I. Goodfellow, Y. Bengio, A. Courville, et al, *Deep learning*. MIT press, 2016.

³<https://github.com/aleju/imgaug>

⁴Results of JSRT and SH datasets

- [2] A. Esteva, B. Kuprel, A. Novoa, et al., "Dermatologist-level classification of skin cancer with deep neural networks," *Nature*, vol. 542, no. 7639, pp. 115–118, 2017.
- [3] S. M. McKinney, M. Sieniek, V. Godbole, et al., "International evaluation of an AI system for breast cancer screening," *Nature*, vol. 577, no. 7788, pp. 89–94, 2020.
- [4] J. Deng, W. Dong, R. Socher, et al., "Imagenet: A large-scale hierarchical image database," in *IEEE Conference on Computer Vision and Pattern Recognition (CVPR)*, pp. 248–255, 2009.
- [5] B. Zhou, A. Lapedriza, A. Khosla, et al., "Places: A 10 million image database for scene recognition," in *IEEE Transactions on Pattern Analysis and Machine Intelligence*, 2017.
- [6] Y. Chen, H. Zhang, Y. Wang, Y. Yang, X. Zhou and Q. M. J. Wu, "MAMA Net: Multi-scale attention memory autoencoder network for anomaly detection," in *IEEE Transactions on Medical Imaging*, vol. 40, no. 3, pp. 1032–1041, 2021.
- [7] Y. Yimin, Q. M. Jonathan, "Multilayer extreme learning machine with subnetwork nodes for representation learning," in *IEEE Transactions on Cybernetics*, vol. 46, pp. 2570–2583, 2016.
- [8] H. Greenspan, B. van Ginneken and R. M. Summers, "Guest editorial deep learning in medical imaging: overview and future promise of an exciting new technique," in *IEEE Transactions on Medical Imaging*, vol. 35, no. 5, pp. 1153–1159, 2016.
- [9] L. Zhang, X. Wang, D. Yang, et al., "Generalizing deep learning for medical image segmentation to unseen domains via deep stacked transformation," in *IEEE Transactions on Medical Imaging*, vol. 39, no. 7, pp. 2531–2540, 2020.
- [10] W. M. Kouw and M. Loog, "A review of domain adaptation without target labels," in *IEEE Transactions on Pattern Analysis and Machine Intelligence*, vol. 43, no. 3, pp. 766–785, 2021.
- [11] T. Dissanayake, T. Fernando, S. Denman, H. Ghaemmaghami, S. Sridharan and C. Fookes, "Domain generalization in biosignal classification," in *IEEE Transactions on Biomedical Engineering*, vol. 68, no. 6, pp. 1978–1989, 2021.
- [12] F. M. Carlucci, A. D'Innocente, S. Bucci, B. Caputo, and T. Tommasi, "Domain generalization by solving jigsaw puzzles," in *IEEE Conference on Computer Vision and Pattern Recognition (CVPR)*, 2019.
- [13] K. Muandet, D. Balduzzi, and B. Schölkopf, "Domain generalization via invariant feature representation," in *International Conference on Machine Learning (ICML)*, pp. 10–18, 2013.
- [14] W. Zuo, X. Peng, L. Shao, D. Prokhorov and H. Bischof, "Guest editorial special issue on discriminative learning for model optimization and statistical inference," in *IEEE Transactions on Neural Networks and Learning Systems*, vol. 30, no. 10, pp. 2894–2897, 2019.
- [15] H. Li, Y. Wang, R. Wan, S. Wang, T. Q. Li, and A. C. Kot, "Domain generalization for medical imaging classification with linear-dependency regularization," in *Conference on Neural Information Processing Systems (NeurIPS)*, 2020.
- [16] A. V. Oprea, M. A. Ikram, M. W. Vernooij and M. D. Bruijne, "Transfer learning improves supervised image segmentation across imaging protocols," in *IEEE Transactions on Medical Imaging*, vol. 34, no. 5, pp. 1018–1030, 2015.
- [17] N. Tajbakhsh, J. Y. Shin, S. R. Gurudu, R. T. Hurst, C. B. Kendall, M. B. Gotway, and J. Liang, "Convolutional neural networks for medical image analysis: full training or fine tuning?," in *IEEE Transactions on Medical Imaging*, vol. 35, no. 5, pp. 1299–1312, 2016.
- [18] V. Cheplyginab, M. Bruijnead, and J. Pluimbc, "Not-so-supervised: A survey of semi-supervised, multi-instance, and transfer learning in medical image analysis," *Medical Image Analysis*, Vol. 54, pp. 280–296, 2019.
- [19] K. He, R. Girshick, and P. Dollar, "Rethinking imagenet pre-training," in *International Conference on Computer Vision (ICCV)*, 2019, pp. 4918–4927.
- [20] K. He, X. Zhang, S. Ren, and J. Sun, "Deep residual learning for image recognition," in *IEEE Conference on Computer Vision and Pattern Recognition (CVPR)*, pp. 770–778, 2016.
- [21] M. Noroozi and P. Favaro, "Unsupervised learning of visual representations by solving jigsaw puzzles," in *European Conference on Computer Vision (ECCV)*, pp. 69–84, 2016.
- [22] R. Zhang, P. Isola, and A. A. Efros, "Colorful image colorization," in *European Conference on Computer Vision (ECCV)*, 2016.
- [23] S. Gidaris, P. Singh, N. Komodakis, "Unsupervised representation learning by predicting image rotations," in *International Conference on Learning Representations (ICLR)*, 2018.
- [24] M. Caron, I. Misra, J. Mairal, et al., "Unsupervised learning of visual features by contrasting cluster assignments," in *Neural Information Processing Systems (NeurIPS)*, 2020.
- [25] J. B. Grill, F. Strub, F. Altché, et al., "Bootstrap your own latent: A new approach to self-supervised learning," in *Neural Information Processing Systems (NeurIPS)*, 2020.
- [26] T. Chen, S. Kornblith, M. Norouzi, et al., "A simple framework for contrastive learning of visual representations," in *International Conference on Machine Learning (ICML)*, pp. 1597–1607, 2020.
- [27] K. He, H. Fan, Y. Wu, et al., "Momentum contrast for unsupervised visual representation learning," in *IEEE Conference on Computer Vision and Pattern Recognition (CVPR)*, pp. 9729–9738, 2020.
- [28] D. Hendrycks, K. Lee, and N. Mazeika, "Using pre-training can improve model robustness and uncertainty," in *International Conference on Machine Learning (ICML)*, 2019, pp. 2712–2721.
- [29] D. Hendrycks, M. Mazeika, and S. Kadavath, D. Song, "Using self-supervised learning can improve model robustness and uncertainty," in *Neural Information Processing Systems (NeurIPS)*, 2019.
- [30] H. Sowrirajan, J. Yang, A. Y. Ng, and P. Rajpurkar, "MoCo-CXR: MoCo pretraining improves representation and transferability of chest X-ray models," in *International Conference on Medical Imaging with Deep Learning (MIDL)*, 2021.
- [31] O. Ronneberger, P. Fischer, and T. Brox, "U-net: Convolutional networks for biomedical image segmentation," in *International Conference on Medical Image Computing and Computer-assisted Intervention*, pp. 234–241, 2015.
- [32] L. Zhang, A. Liu, J. Xiao and P. Taylor, "Dual encoder fusion U-Net (DEFU-Net) for cross-manufacturer chest X-ray segmentation," in *International Conference on Pattern Recognition (ICPR)*, pp. 9333–9339, 2021.
- [33] C. Chen, Y. Zhu, G. Papandreou, et al., "Encoder-decoder with atrous separable convolution for semantic image segmentation," in *European conference on computer vision (ECCV)*, pp. 801–818, 2018.
- [34] H. Zhao, J. Shi, X. Qi, X. Wang, and J. Jia "Pyramid scene parsing network," in *IEEE Conference on Computer Vision and Pattern Recognition (CVPR)*, pp. 2881– 2890, 2017.
- [35] D. Qin et al., "Efficient medical image segmentation based on knowledge distillation," in *IEEE Transactions on Medical Imaging*, 2021.
- [36] R. Rashid, M. U. Akram, and T. Hassan, "Fully convolutional neural network for lungs segmentation from chest X-rays," in *International Conference Image Analysis and Recognition (ICIAR)*, pp. 71–80, 2018.
- [37] S. Candemir, S. Jaeger, K. Palaniappan K, et al., "Lung segmentation in chest radiographs using anatomical atlases with nonrigid registration," in *IEEE Transactions on Medical Imaging*, vol. 33, no. 2, pp. 577–590, 2013.
- [38] I. Goodfellow, J. Pouget-Abadie, M. Mirza, B. Xu, D. Warde-Farley, S. Ozair, A. Courville, and Y. Bengio, "Generative adversarial nets," in *Conference on Neural Information Processing Systems (NeurIPS)*, 2014, pp. 2672–2680.
- [39] D. P. Kingma, and M. Welling, "Auto-Encoding variational Bayes," in *International Conference on Machine Learning (ICML)*, 2014.
- [40] T. W. Cenggoro, "Deep learning for imbalance data classification using class expert generative adversarial network," *Procedia Computer Science*, vol. 135, pp. 60–67, 2018.
- [41] A. Newell, J. Deng, "How useful is self-supervised pretraining for visual tasks?" in *IEEE Conference on Computer Vision and Pattern Recognition (CVPR)*, 2020, pp. 7345–7354.
- [42] I. Tolstikhin, O. Bousquet, S. Gelly, et al., "Wasserstein auto-encoders," in *International Conference on Learning Representation (ICLR)*, 2018.
- [43] S. Kolouri, G. Rohde, H. Hoffmann, "Sliced wasserstein distance for learning Gaussian mixture models," in *Computer Vision and Pattern Recognition (CVPR)*, 2018, pp. 3427–3436.
- [44] A. Myronenko A, "3D MRI brain tumor segmentation using autoencoder regularization," in *International MICCAI Brainlesion Workshop*, 2018, pp. 311–320.
- [45] F. Milletari, N. Navab, S. A. Ahmadi, "V-net: Fully convolutional neural networks for volumetric medical image segmentation," in *International Conference on 3D Vision (3DV)*, 2016.
- [46] S. D. Kermany, M. Goldbaum, W. Cai, et al., "Identifying medical diagnoses and treatable diseases by image-based deep learning," *Cell*, vol. 172, no. 5, pp. 1122–1131, 2018.
- [47] S. Jaeger, S. Candemir, S. Antani, et al., "Two public chest X-ray datasets for computer-aided screening of pulmonary diseases," *Quant Imaging Med Surg*, vol. 4, no. 6, pp. 475–477, 2014.
- [48] J. Shiraiishi, S. Katsuragawa, J. Ikezoe et al., "Development of a digital image database for chest radiographs with and without a lung nodule: Receiver operating characteristic analysis of radiologists' detection of pulmonary nodules." *AJR*, vol. 174, pp. 71–74, 2000.